

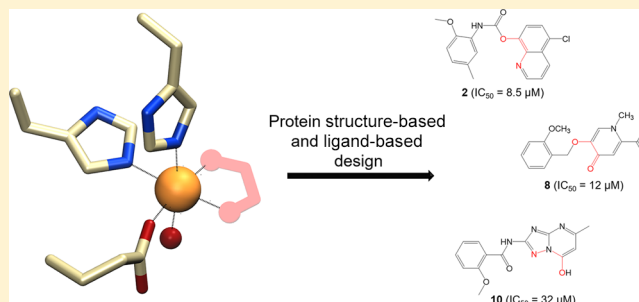
In Silico Identification of JMJD3 Demethylase Inhibitors

C. Esposito,^{ib} L. Wiedmer, and A. Caflisch*^{ib}

Department of Biochemistry, University of Zurich, Winterthurerstrasse 190, CH-8057 Zurich, Switzerland

S Supporting Information

ABSTRACT: In the search for new demethylase inhibitors, we have developed a multistep protocol for *in silico* screening. Millions of poses generated by high-throughput docking or a 3D-pharmacophore search are first minimized by a classical force field and then filtered by semiempirical quantum mechanical calculations of the interaction energy with a selected set of functional groups in the binding site. The final ranking includes solvation effects which are evaluated in the continuum dielectric approximation (finite-difference Poisson equation). Application of the multistep protocol to JMJD3 jumonji demethylase has resulted in a dozen low-micromolar inhibitors belonging to five different chemical classes. We have solved the crystal structure of JMJD3 inhibitor 8 in the complex with UTX (a demethylase in the same subfamily as JMJD3) which validates the predicted binding mode. Compound 8 is a promising candidate for future optimization as it has a favorable ligand efficiency of 0.32 kcal/mol per nonhydrogen atom.



INTRODUCTION

Jumonji histone lysine demethylases (KDMs) are iron- and 2-oxoglutarate (OGA)-dependent dioxygenases.¹ They catalyze the removal of methyl groups from methylated lysines in histone tails, and according to the demethylation site on the histone, they either activate or suppress transcription.^{2–4} JMJD3 (also called KDM6B), together with UTX (also called KDM6A) and UTY, belongs to the KDM6 subfamily of jumonji demethylases, which catalyze specifically the demethylation of di- and trimethylated lysine 27 of the histone 3 tail (H3K27me_{2/3}).⁵ JMJD3 is considered a potential pharmaceutical target⁶ because it has an influence on the expression of genes⁷ that are involved in inflammatory response,^{8,9} neurodegenerative diseases,¹⁰ and T-cell acute lymphoblastic leukemia (T-ALL).^{11,12}

To date, the most potent inhibitor of JMJD3 is the compound GSK-J1, which is 5- to 10-fold more selective for KDM6 relative to the KDM5 subfamily.⁹ Its cell-permeable prodrug GSK-J4 shows reduced activity and no selectivity in *in vitro* and *in vivo* assays.¹³ Structure–activity relationship (SAR) studies of GSK-J1 led to the identification of thiazolo-, pyrazolo-, and triazolopyrimidine derivatives, which showed similar or reduced potency.¹⁴ As claimed in a recent article by Nowak et al.,¹⁵ although potent inhibitors have been identified for most KDM subfamilies, the identification of selective and cell-permeable inhibitors remains a challenge. McAllister et al.¹⁶ have reviewed KDM inhibitors developed since 2014 and pointed out that the vast majority of the identified inhibitors are OGA competitors and are all derivatives of a reduced number of metal-chelating fragments. Taken together, these studies indicate the need for developing novel JMJD3 inhibitors.

Protein structure-based computer-aided methods have been applied successfully for hit discovery and lead optimization.^{17,18}

In contrast, metallo-proteins are considered difficult targets for *in silico* drug discovery because of the difficulty in modeling the metal–ligand bonds. First, the optimal orientation of metal–ligand complexes within a protein is not well reproduced by docking programs because of the complexity of the coordination geometries that transition metals can exploit.^{19,20} Recent efforts have been devoted to the development of *ad hoc* programs for zinc-dependent proteins, as AutoDock4Zn²¹ and MpSDockZn,²² but their usage is limited to this class of proteins. Second, commonly used force field-based, empirical²³ or knowledge-based²⁴ scoring functions do not account for electronic effects, and consequently, they are not able to capture the nature of organometallic bonds, preventing a correct ranking of ligand poses.^{25–27} More accurate binding energies from quantum mechanics (QM)-based scoring functions^{20,27–29} seem to correlate with experimental data, but the application of these methodologies to high throughput screening is restricted by the computational cost. These limitations in the modeling of metal–ligand binding explain the general preference for experimental techniques compared to *in silico* studies for drug discovery of jumonji demethylases.^{30–32}

Here, we introduce a high-throughput docking protocol for the identification of KDMs inhibitors. The multistep protocol makes use of a classical force field and semiempirical QM calculations. We report on two applications of the virtual screening protocol for the identification of JMJD3 inhibitors. The first campaign focused on identifying derivatives of known KDM iron-chelating scaffolds, while the goal of the second screening was to find potent compounds containing novel scaffolds.

Received: August 10, 2018

Published: September 18, 2018

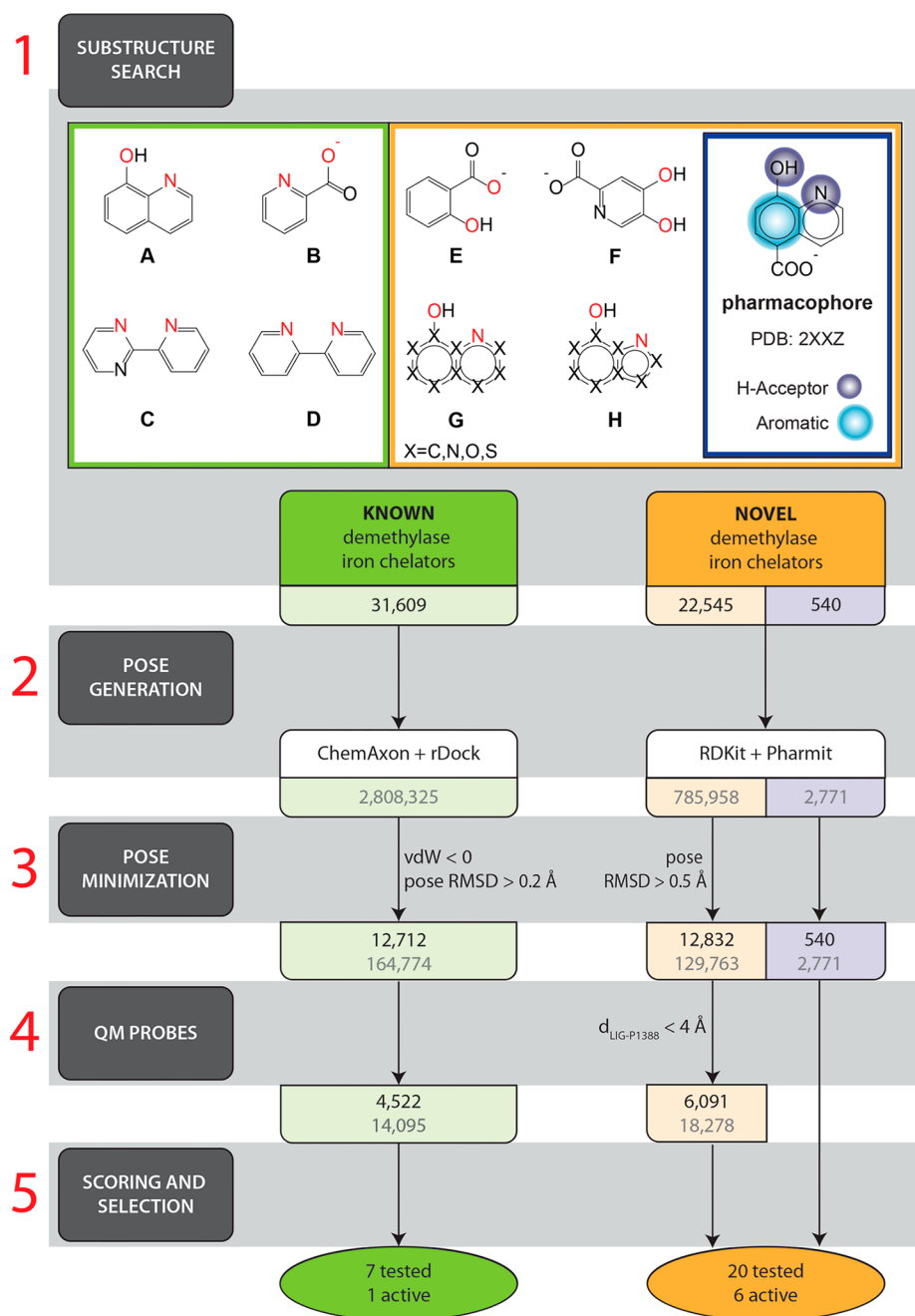


Figure 1. Schematic illustration of the five-step procedure for virtual screening. Atoms that are supposed to chelate the metal are highlighted in red. The flowchart on the left illustrates the high-throughput screening of derivatives of iron-chelating scaffolds A–D reported previously as demethylase inhibitors (green). The flowchart on the right summarizes the virtual screening of potentially novel JMJD3 inhibitors (orange). The screening of the novel scaffolds started from a focused library assembled by substructure search of fragments E–H (orange) and 540 compounds from a pharmacophore-based search (purple). Compounds are considered active if they show an $IC_{50} < 100 \mu\text{M}$ in the AlphaScreen assay. The count in the green oval does not include the four actives obtained by expansion of the hit identified in the first campaign.

METHODS

Multistep Protocol for *in Silico* Screening. The virtual screening workflow was first validated on known KDM scaffolds (compounds A–D in Figure 1, flowchart shown in green) and subsequently adapted for the identification of novel JMJD3 inhibitors. The second campaign comprised the screening of derivatives of potential iron-chelating fragments (E–H in Figure 1, flowchart in orange) and the screening of compounds that matched the pharmacophore model (flowchart in purple in Figure 1) derived from the crystallographic structure of JMJD3

in complex with 5-carboxy-8-hydroxyquinoline (5C8HQ, PDB code: 2XXZ).³³ In the following, we first describe the five steps in common to the two *in silico* screenings and then present the details of each of the two campaigns. The five steps are as follows:

- (1) Preparation of the screening library containing only potential bidentate metal-binding ligands. The library of known iron-chelating scaffolds A–D (Figure 1) was assembled by a substructure search in the 2012 version of the ZINC “all-purchasable” database, which yielded

- 31,609 compounds. The library of novel scaffolds included the 22,545 compounds identified by a substructure search in the ZINC database using fragments E–H as the query (Figure 1) and 540 molecules from the ChemDiv database obtained by pharmacophore similarity to 5C8HQ. The pharmacophore model consisted of two hydrogen bond acceptors at the positions of the iron-coordinating atoms (*viz.*, hydroxyl oxygen and pyridine nitrogen) and an aromatic group centered on the benzene ring of 5C8HQ (Figure 1 and Figure S1).
- (2) Pose generation by substructure alignment to ligands in available holo crystal structures. This step started with the generation of an ensemble of conformers for each of the compounds and was followed by the docking of the conformers into the protein structure. To this purpose, tethered docking and pharmacophore-based docking were used for the first and second *in silico* screening, respectively. In the first campaign, tethered docking consisted of restraining the chelating substructure of conformers of KDM inhibitor derivatives to the substructure coordinates of the parent compounds obtained from crystal structures. In the second campaign, pharmacophore-based docking^{34,35} was used to generate poses of compounds containing diverse iron-binding moieties. This implied the generation of a pharmacophore query in terms of features that could ensure optimal interactions with the metal. The set of pharmacophore features was chosen on the basis of the crystallographic structure of 5C8HQ (Figure S1). Afterward, the ensemble of conformers contained in the library of novel compounds (orange and purple flowcharts in Figure 1) was searched for conformers matching the pharmacophore query. The prebuilt ChemDiv database available on the Pharmit server³⁶ provides pregenerated conformers, while conformers of derivatives of scaffolds E–H (orange flowchart in Figure 1) were generated using RDKit (see second *in silico* screening).
 - (3) Pose minimization by CHARMM.³⁷ During minimization, the protein, iron, and water molecules directly bound to the iron were maintained fixed. The fully compatible CHARMM36³⁸ force field and CHARMM General Force Field (CGenFF)³⁹ were used for the protein and small molecules, respectively. A Coulombic energy with distance-dependent dielectric constant (4r) was employed as an efficient approximation of the solvent-screening of electrostatic interactions.⁴⁰
 - (4) Estimation of interaction energies at the semiempirical PM7 level between small molecules and individual polar groups (probes) in the binding pocket.⁴¹ The interaction energy between a probe and the potential ligands was evaluated as $IE_{probe} = H_{ligand-probe} - H_{ligand} - H_{probe}$ where H is the formation enthalpy calculated by MOPAC⁴² with the PM7 Hamiltonian.⁴³ Small molecular fragments were designed to model the local electronic structure of the binding site (Table S1) and approximate the polar groups of residues that interact directly with GSK-J1 (Figure S2A, PDB code: 4ASK) and 5C8HQ (Figure S2B, PDB code: 2XXZ). Probes containing at least one dihedral angle were considered partially flexible (the probe atoms optimized during the PM7 minimization are highlighted in boldface in Table S1). The conformations of the compounds minimized by CHARMM in step 3 were kept fixed during the IE_{probe} evaluation. The thresholds used for filtering the compounds were selected on the basis of the IE_{probe} distributions and the IE_{probe} of the positive controls GSK-J1 and 5C8HQ (Table S1 and Figures S3–S4).
 - (5) Pose scoring by the CHARMM36/CGenFF energy function which consists of van der Waals interaction and electrostatics with implicit solvent treatment (continuum-dielectric approximation) as in previous works.^{40,44} The electrostatic contribution to the binding free energy was calculated by the finite-difference Poisson–Boltzmann module in CHARMM.⁴⁵ This contribution is evaluated by subtracting the electrostatic energy of the unbound protein and unbound ligand from the energy of the complex. An ionic strength of zero was used so that the Poisson–Boltzmann equation reduces to the Poisson equation.
- Geometric and electronic effects due to the presence of the iron ion in the active site were dealt with as follows. First, to ensure the maintenance of the octahedral coordination, poses were generated by alignment of the iron-chelating moiety to the known inhibitors scaffold according to available co-crystal structures (step 2). Second, electronic effects were considered during the pose minimization and binding energy evaluation by CHARMM (steps 3 and 5, respectively). Several approaches have been developed to model metal coordination bonds in all-atom force fields, including the bonded model,^{46,47} nonbonded model,^{48,49} and dummy cation model.^{50–52} Here, a nonbonded approach was used, where bonds were considered as ionic, but the charge of the iron was redistributed on the neighboring residues to partially take into account electronic effects. In particular, the formal charge on the iron ion was set to 1+ instead of 2+, while the total formal charge of the iron complex was kept constant by protonating the glutamate directly bound to the metal (see below).
- First Screening Campaign: High-Throughput Docking of Derivatives of Known Scaffolds.** Four scaffolds A–D (Figure 1) from known metal-chelating KDM inhibitors¹⁶ were selected and used for a substructure search in the 2012 version of the ZINC “all purchasable” database, yielding a focused library of 31,609 compounds. ChemAxon software⁵³ was used for predicting pK_a and tautomeric states, as previously reported.⁴⁰ Considering that hydroxyl groups bind metals in the ionic form,^{54,55} derivatives of fragment A containing the phenolic moiety were deprotonated using Open Babel 2.3.2.⁵⁶ For each compound, 10N molecular conformers were generated by ChemAxon, where N is the number of rotatable bonds. Derivatives of fragments A and C were tethered according to the available JMJD3/inhibitor co-crystal structures by rDock⁵⁷ (PDB codes: 2XXZ and 4ASK). Since no crystal structure was available for fragment B in complex with JMJD3, its pose was predicted by structure alignment of the JMJD2D/2,4-pyridinedicarboxylic acid complex (PDB code: 4D6Q) to the backbone atoms of 4ASK. The binding mode of scaffold D, whose crystallographic structure was unavailable, was predicted based on similarity to the GSK-J1 chelating substructure (scaffold C).
- The tethered conformers were parametrized using the MATCH⁵⁸ program and subsequently minimized by CHARMM.³⁷ The CHARMM36 force field³⁸ was employed for the protein. Electrostatic effects due to the presence of the ferrous ion (2+) in the binding site were modeled by redistributing the positive charge between the iron itself (1+), and the protonated glutamate directly bound to it (0). The iron-chelating scaffold

was constrained to prevent the distortion of the octahedral coordination. The two water molecules coordinating the iron were considered as part of the protein and maintained fixed. Poses were minimized with rigid protein through 500 steps of steepest descent minimization and 10,000 steps of conjugate gradient minimization. The minimized poses with steric repulsion were discarded by filtering out ligands with a positive van der Waals energy. Conformers generated by ChemAxon were not necessarily in a local minimum, and minimization led to redundant poses. In order to remove these redundant poses, ligand conformers were extracted from the minimized protein–ligand complex and clustered in dihedral angle space. Hierarchical clustering⁵⁹ was carried out by CAMPARI (version 2, <http://campari.sourceforge.net/>) with a threshold radius of 2°.

The number of compounds (164,774 poses of 12,712 molecules) was significantly reduced by filtering using the QM probes.⁴¹ According to the crystallographic structures of JMJD3 in complex with GSK-J1, 5C8HQ, and OGA (PDB codes: 4ASK, 2XXZ, and 2XUE, respectively), the side chain of Tyr1379 forms hydrogen bonds with JMJD3 ligands, while Lys1381 and Asn1400 are located at the bottom of the active site and interact with the carboxyl group of the ligands. Asn1393 is located at the entrance of the binding pocket. Thus, probes relative to the side chains of Tyr1379, Lys1381, Asn1393, and Asn1400 were selected for filtering. Cutoff energies were chosen taking into account the IE_{probe} distributions (Figure S3) and the IE_{probe} values for two known inhibitors, GSK-J1 and 5C8HQ (Table S1 and Figure S2), *viz.*, $IE_{Tyr1379} < -1$ kcal/mol, $IE_{Lys1381} < -2$ kcal/mol, $IE_{Asn1393} < 5.5$ kcal/mol, and $IE_{Asn1400} < 0$ kcal/mol. The first cutoff value corresponds to the interaction energy between GSK-J1 and the Tyr1379 probe. Cutoff values employed for $IE_{Lys1381}$ and $IE_{Asn1400}$ could not be selected on the basis of the known inhibitor energy values because, due to the negatively charged carboxyl group, both GSK-J1 and 5C8HQ interact more favorably with Lys1381 and Asn1400 than the majority of the screened compounds (Figure S3). Therefore, cutoff energies of -2 and 0 kcal/mol were, respectively, chosen for $IE_{Lys1381}$ and $IE_{Asn1400}$ with the purpose of keeping conformers interacting favorably with the two probes. At last, since Asn1393 is located in close proximity to the scaffold of GSK-J1 (the closest distance between GSK-J1 heavy atoms and Asn side chain nitrogen atom is 3.55 Å), the filter $IE_{Asn1393} < 5.5$ kcal/mol was chosen to discard only derivatives of scaffolds C and D having substituents giving unfavorable interactions to Asn1393.

The selected filters based on QM probes reduced the number of poses by about 12-fold and the number of compounds by a factor of 3. The remaining 14,095 poses of 4522 compounds were ranked according to the binding energy evaluated with CHARMM36/CGenFF, *i.e.*, van der Waals energy and electrostatics in implicit solvent using the continuum dielectric approximation. The finite-difference Poisson equation as implemented in the pbeq module of CHARMM⁴⁵ was used with dielectric constants of solute and solvent equal to 2 and 78.5, respectively.

Finally, seven of the 20 top molecules according to the total energy were selected for experimental validation (compound I in Table 1 and compounds S1–S6 in Figure S6).

Second Screening Campaign: Pharmacophore Search of Novel Potential Binders. Fragments E and F (Figure 1) were reported in a previous study that investigated the binding of molecular fragments to a panel of metallo-enzymes.⁶⁰ These two fragments were selected from a set of 96 fragments because they selectively inhibited 76% to 100% of the activity of two nonheme iron dependent enzymes, anthrax lethal factor and

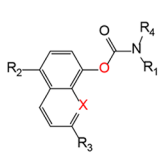
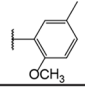
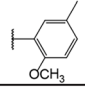
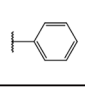
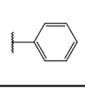
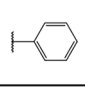
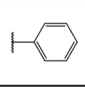
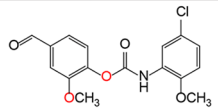
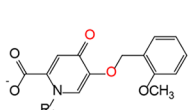
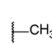
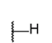
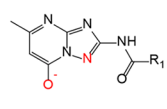
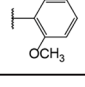
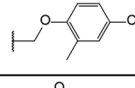
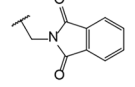
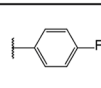
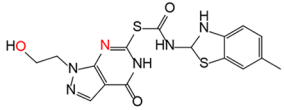
5-lipoxygenase. Fragment F was derivatized introducing a carboxyl group *ortho* to the pyridine nitrogen, with the aim of identifying ligands giving electrostatic interactions to Lys1381. Fragments G and H are analogues of 8HQ as they retain the bicyclic aromatic ring substructure and the metal-binding mode of the parent fragment through the phenolic oxygen and aromatic nitrogen heteroatoms. In contrast to 8HQ, G and H were designed to contain additional heteroatoms (oxygen, nitrogen, or sulfur) in the bicyclic aromatic ring, with the purpose of fine-tuning the electronic properties of the scaffolds^{61,62} and eventually identifying compounds containing novel KDM metal-binding heterocycles.

The combined library of 23,085 compounds (540 from the Pharmit search of the ChemDiv library and 22,545 from substructure search using scaffolds E–H) was screened against JMJD3 (PDB code: 2XXZ). As described above, protonation and tautomeric states were predicted using ChemAxon plugins. The phenolic metal-chelating moieties were deprotonated using Open Babel. The 2771 conformers of the 540 compounds from ChemDiv were minimized by CHARMM and ranked according to the total free energy of binding. Instead, the remaining 129,763 poses of 12,832 compounds from the ZINC database underwent the procedure applied to the first campaign. Unlike in the first campaign, conformers were generated by the RDKit standard conformer ensemble generator⁶³ and minimized within RDKit using the Universal Force Field (UFF)⁶⁴ because of its accuracy in reproducing protein-bound ligand conformations.⁶³ The ensemble comprised a maximum of 2000 conformers with an interconformer RMSD limit of 2.0 Å. Subsequently, the library was uploaded on the web server Pharmit. The Pharmit interface was used to define the pharmacophore model (see step 1) and to filter out conformers that did not fit the pharmacophore map. Poses were minimized by CHARMM and clustered by CAMPARI with an all-atom RMSD cutoff of 0.5 Å. To bias the search toward selective ligands, poses at a distance higher than 4 Å from Pro1388 were filtered out as Pro1388 is located in a poorly conserved subpocket of the active site. The side chain of Pro1388 interacts with Pro30 of the histone tail, a nonconserved sequence stretch that starts three residues downstream of the methylated histone lysine H3K27 (Figure S5).

The values of interaction energy between QM probes and compounds were evaluated at the semiempirical PM7 level by MOPAC (Figures S2 and S4). Probes relative to Gln1377, Tyr1379, and Gly1435 were selected for filtering. Gln1377 and Gly1435 are poorly conserved residues among the jumonji demethylase family and were chosen as filters in order to improve ligand selectivity. The interaction energy between the selected probes and the known inhibitors are reported in Table S1. The adopted cutoff energies are $IE_{Gln1377} < -0.3$ kcal/mol, $IE_{Tyr1379} < -0.6$ kcal/mol, and $IE_{Gly1435} < 0.5$ kcal/mol. Cutoff values employed for $IE_{Gln1377}$ and $IE_{Gly1435}$ were selected on the basis of the known inhibitors interaction energy values. Instead, a value of -0.6 kcal/mol was chosen as cutoff for $IE_{Tyr1379}$ to decrease the number of conformers 6-fold. In this case, the interaction energy values between Tyr1379 and the known inhibitors were more favorable than the values for the majority of the screened compounds (Figure S4).

The remaining 18,278 poses of 6091 compounds were ranked according to the CHARMM36/CGenFF binding energy with implicit solvent, as detailed above. In this campaign, the effect of charge redistribution in the binding site was further investigated by testing three charge distributions, Fe(2+)-Glu1392(1-), Fe(1+)-GluH(0), and Fe(0)-GluH(0). The predictive ability of

Table 1. *In Vitro* Results for 14 Compounds Tested by Dose–Response AlphaScreen Assay^a

Metal Chelator	R ₁	R _{2,3,4} X	Compound	IC ₅₀ (μM)	LE (kcal/mol per HA)	In silico procedure
		X = N	1	15 17	0.29 0.28	Tethering to PDB substructure
		R ₂ = Cl X = N	2	5 12	0.30 0.28	SAR by substructure search
		X = N	3	95	0.28	
		R ₃ = CH ₃ X = N	4	62	0.27	
		R ₄ = CH ₃ X = N	5	> 200		
		X = C	6	> 200		
			7	46	0.26	SAR by substructure search and pharmacophore based pose generation
		PDB code: 6FUL	8	12	0.32	Substructure search and pharmacophore based pose generation
			9	76	0.28	
			10	32	0.28	Pharmacophore based search and pose generation
			11	35 97	0.25 0.23	
			12	32	0.24	
			13	150	0.25	
			14	77	0.20	

^aOnly nonhydrogen atoms are specified for R_{2,3,4}. Compounds **1**, **2**, and **11** were measured twice, and both IC₅₀ values are shown. The purity of all compounds was >95% as reported by the vendors.

the scorings was quantified using the area (AUC) under the receiver operating characteristic (ROC) curve, which gave values of 0.48, 0.68, and 0.34, respectively. Thus, the total binding energy calculated according to the charge redistribution Fe(1+)-GluH(0) was used for ranking and selecting compounds for *in vitro* validation (Figure S7A). The 10 inhibitors used as true positives include eight previously disclosed ligands and compounds **1** and **2** (Figure S7B). A total of 8 and 12 molecules were selected for experimental validation from the substructure search (compounds **8** and **9** in Table 1 and S7–S12 in Figure S8)

and pharmacophore search (compounds **10–14** and S13–S19), respectively.

AlphaScreen Experiment. AlphaScreen measurements were carried out at Reaction Biology Corporation (USA). AlphaScreen is a bead-based proximity assay. When the donor bead is illuminated at 680 nm, it converts ambient oxygen to singlet oxygen. Singlet oxygen has a half-life of 4 μs, in which it can diffuse approximately 200 nm, in solution. If the acceptor bead is within 200 nm from the donor bead, an energy transfer occurs resulting in light production at 520–620 nm. Donor and

acceptor beads were coated by streptavidin and an antibody against the demethylated histone tail (H3K27me1/2), respectively. In the presence of inhibitory compounds, JMJD3 was prevented from catalyzing the demethylation reaction, leading to loss of the luminescent signal. Enzyme activity was measured with respect to DMSO control.

X-ray Crystallography. Protein Production and Crystallization. The JMJD3 plasmid was a gift from Nicola Burgess-Brown (Addgene plasmid # 39069). The UTX (880-1401) plasmid cloned into pET47b (Merck) was kindly provided by the RIKEN Systems and Structural Biology Center. UTX was expressed and purified according to the protocol published by Sengoku and Yokoyama.⁶⁵ In brief, transformed cells were harvested, and the pellet was suspended in 20 mM Tris-HCl buffer (pH 7.5), 0.5 M NaCl, 10 mM 2-mercaptoethanol, 0.1 mM phenylmethylsulfonyl fluoride (PMSF), 20 mM imidazole, 1% Triton X-100, and 0.1 mg/mL lysozyme. His-tagged protein was purified using a prepacked HisTrap FF column (GE Healthcare: 17525501). The polyhistidine tags were cleaved by the His-tagged HRV3C protease during an overnight dialysis (20 mM Tris-HCl pH 7.5, 500 mM NaCl, 10 mM 2-mercaptoethanol, 10% glycerol). UTX was further purified by a second HisTrap FF column and a size exclusion chromatography using a HiLoad 16/600 Superdex 200 column (GE Healthcare). The purified protein was concentrated to 10–12 mg/mL in a 20 mM Tris-HCl buffer (pH 7.5) containing 200 mM NaCl and 0.5 mM TCEP. Crystals were grown by vapor diffusion at 4 °C using a crystallization buffer containing 0.1 M Tris-HCl (pH 8.5), Li₂ SO₄ (0.15–0.25 M), and PEG 3350 (20–25% w/v). Since this construct showed expression and aggregation problems, a different UTX (880-1401) plasmid cloned into pOPIN F vector was used for further crystallization experiments. This plasmid was a gift from the Kristensen group of the University of Copenhagen.⁶⁶ The protein was expressed in BL21 and purified as described in the published protocol.⁶⁶ Unlike the published protocol, a HiLoad 16/600 Superdex 200 column was used for size exclusion chromatography. The protein was concentrated to 12 mg/mL, and crystals were obtained in the same conditions as reported above using micro-seeding. Apo crystals were harvested and soaked overnight in the reservoir buffer supplemented with the compounds of interest, 1 mM MnCl₂ and 20% ethylene glycol. GSK-J1 and compound 8 were tested at 5 and 10 mM, respectively, while 5C8HQ was tested at saturating conditions. Soaked crystals were frozen in liquid nitrogen.

Data Collection and Structure Solution. Diffraction data were collected at the Swiss Light Source, Paul Scherrer Institute (Villigen, Switzerland), beamlines PXI and PXIII. Data were processed with XDS.⁶⁷ Structures were solved by molecular replacement with Phaser⁶⁸ using PDB 3AVS as search model. Initial models were refined iteratively with Phenix⁶⁹ and manual model building with COOT.⁷⁰ Crystal data collection and refinement statistics are summarized in Table S3.

RESULTS

Virtual Screening of Derivatives of Known Metal-Chelating Scaffolds. The first *in silico* screening consisted of the high-throughput tethered docking of a focused library of about 30,000 derivatives of four known KDM inhibitors (fragments A–D, Figure 1). Seven molecules were selected for *in vitro* testing by the AlphaScreen assay (see Methods). Compound 1, which is a derivative of fragment A, inhibited JMJD3 with an IC₅₀ of 16 μM (dose–response curves are shown in

Figure S9). The remaining six molecules, compounds S1–S6 (Figure S6), were not active in the dose–response assay at the highest tested concentration of 200 μM (Table S2).

Structure–activity Relationship (SAR). On the basis of hit 1, the six compounds 2–7 were tested for exploration of the SAR (structures are shown in Figure 1 and Figure S10 and dose–response curves in Figure S9). The derivatives 2–4 were identified by substructure search of the 8-quinoliny phenyl-carbamate substructure in the ZINC “all-purchasable” database (version 2012). Compounds 5 and 6 were chosen as negative controls to verify that even minor modifications of the chemical groups directly involved in the binding to the metal prevents JMJD3 inhibition. Compound 7 was identified by using the nonquinolinic substructure of compound 1 in the substructure search. The substructure search of the phenyl carbamate group in the ZINC library retrieved 36,831 molecules. To screen only novel potential bidentate metal-binders, the size of this chemical library was reduced to 1836 molecules by filtering out 8-hydroxyquinoline (8HQ) derivatives and preserving only compounds containing a heteroatom (nitrogen, oxygen, or sulfur atoms) at a distance of three bonds from the carbamate oxygen binding to the iron. Conformers and poses of these 1836 compounds were generated as described in Methods for the second *in silico* screening. A total of 2086 conformers of 1675 compounds were parametrized using the CGenFF force field³⁹ and minimized by CHARMM. Compounds were ranked according to the total free energy of binding, and only the top ranked compound (7) was selected for experimental validation.

The results of the SAR study are consistent with the predicted poses (Figure 2, Table 1). Compounds 2–4 are 8-quinoliny phenylcarbamate derivatives and differ from hit 1 in substituents on either the 8HQ or the benzene ring. Compound 2, which contains a chlorine atom at R₂, is slightly more potent than the original hit 1. Compound 3, which lacks the functional groups in positions 2 and 5 of the benzene ring, shows a 6-fold decrease in potency compared to hit 1. According to the predicted binding pose (Figure 2A), the methoxy oxygen is involved in an intramolecular hydrogen bond to the nitrogen atom of the carbamate group and an intermolecular hydrogen bond to the water molecule in the octahedral plane of the iron coordination. Compound 4 shows an IC₅₀ of 62 μM, but the difference with respect to compound 3 is within the error of the measurement. The additional methyl group at position R₃ of compound 4 is predicted to point into a hydrophobic subpocket and interact with the side chain of Ile1464 (Figure 2C). The carbamate group of compounds 1–4 might coexist in two isomer conformations, *syn* and *anti*.⁷¹ As an example, alternative binding modes of compound 1 are shown in Figure 2B.

The negative controls 5 and 6 (at 200 μM) did not show any inhibitory activity against JMJD3 as expected. The replacement of the chelating pyridine nitrogen atom with a carbon atom might have prevented the binding to the iron (compound 6), while the methyl group as substituent at R₄ (compound 5) might have disrupted the hydrogen bond with the water in the octahedral plane of the metal (Figure 2D). Finally, the replacement of 8HQ with vanillin led to a 3-fold weaker inhibition for compound 7 versus the original hit 1, although a direct comparison is not possible because of the difference in the substituent at position 5 of the benzene ring which is a methyl and chlorine in hit 1 and derivative 7, respectively.

Virtual Screening To Identify Novel Metal-Chelating Inhibitors. The second screening campaign made use of a focused library of 23,085 molecules containing novel iron-chelating

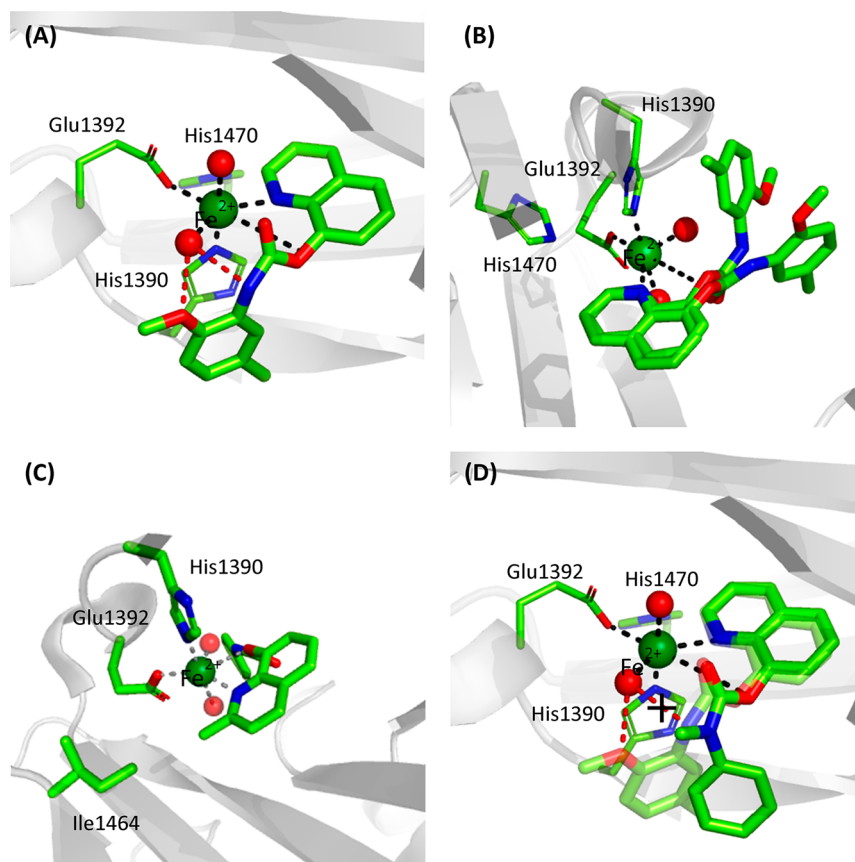


Figure 2. Predicted binding modes of compounds identified by the first *in silico* screening campaign. Poses were generated by tethered docking and minimized using CHARMM (see [Methods](#) for details). During minimization, the protein, iron, and two water molecules were kept fixed. Thus, the minimization of the ligand coordinates might have resulted in a slight distortion of the metal-coordination geometry. (A) Compound 1 coordinates the catalytic metal with the pyridine nitrogen and the phenolic oxygen, as enforced by the tethered docking approach. (B) Possible binding modes of compound 1 in the *syn*-isomer and *anti*-isomer conformations. (C) The methyl group of the 8HQ scaffold of compound 4 is predicted to interact with the side chain of Ile1464. (D) The overlap between the poses of compound 1 in *syn* conformation (lighter green) and the negative control 5 suggests that the methyl group on the carbamate nitrogen would prevent the hydrogen bond to the chelating water. Metal–ligand bonds are shown in black or gray, and water-mediated bonds are shown in red. The color of the carbon atoms and catalytic metal in this figure and the following ones is consistent with the color scheme used for the different screening campaigns (see [Figure 1](#)).

moieties (scaffolds E–H and pharmacophore search in [Figure 1](#), see also [Methods](#)). A total of 20 molecules were selected for experimental validation, and six of them (compounds 8–12 and 14, [Table 1](#)) showed $IC_{50} < 100 \mu\text{M}$ in dose–response measurements ([Figure S11](#)). These compounds contain three novel iron-chelating moieties, which to the best of our knowledge have never been reported to bind jumonji KDM. The 2-carboxy-4-oxo-pyridines derivatives 8 ($IC_{50} = 12 \mu\text{M}$) and 9 ($IC_{50} = 76 \mu\text{M}$) differ only by the methyl group on the pyridine nitrogen. The crystal structure of the complex with compound 8 shows that, as predicted by the pharmacophore-based pose, the *N*-methyl substituent extends into a small hydrophobic subpocket formed by the side chains of Tyr1379 and Ala1482 ([Figure 4D](#)). Since compounds 8 and 9 contain one and two ionizable groups, respectively, we characterized tautomeric and protonation equilibria using ChemAxon ([Figure S15](#)). The preferred state of these compounds is shown in [Table 1](#) and corresponds to the one employed throughout the virtual screening procedure (see [Methods](#)).

Compounds 10–13 are [1,2,4]triazolo[1,5-*a*]pyrimidin-7-ol derivatives and inhibit JMJD3 with an IC_{50} of 30–70 μM or about 150 μM for compound 13 ([Table 1](#)). The predicted poses show direct metal–ligand binding ([Figure 3](#)). The R_1 moiety of these compounds points toward the solvent ([Figure 3B](#)), which

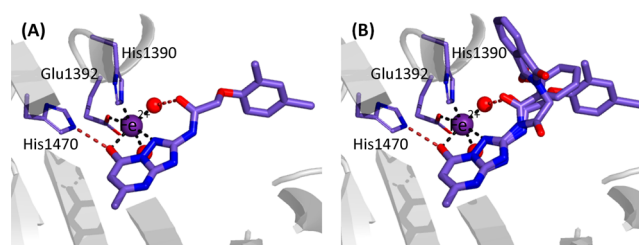


Figure 3. Predicted binding modes of compounds identified by the second docking campaign. Poses were generated by pharmacophore docking using Pharmit. The pharmacophore model was built on the basis of the crystal structure of the JMJD3/SC8HQ complex (see [Figure S2](#)). (A) Predicted binding mode of compound 11. (B) Overlap between the docked poses of compounds 10, 11, and 12.

is congruent with their very similar potencies. The remaining 13 compounds, seven identified by pharmacophore similarity to SC8HQ (S13–S19, [Figure S8](#)) and six derivatives of scaffold H (S7–S12, [Figure S8](#)), were not active at a concentration of 500 μM ([Table S2](#)).

Active Compounds Are Not PAINS. The 12 active compounds were analyzed for the presence of PAINS (pan-assay interference compounds)⁷² and aggregator substructures⁷³ using the FAF-Drugs4^{74,75} and the Aggregator Advisor⁷⁶ Web

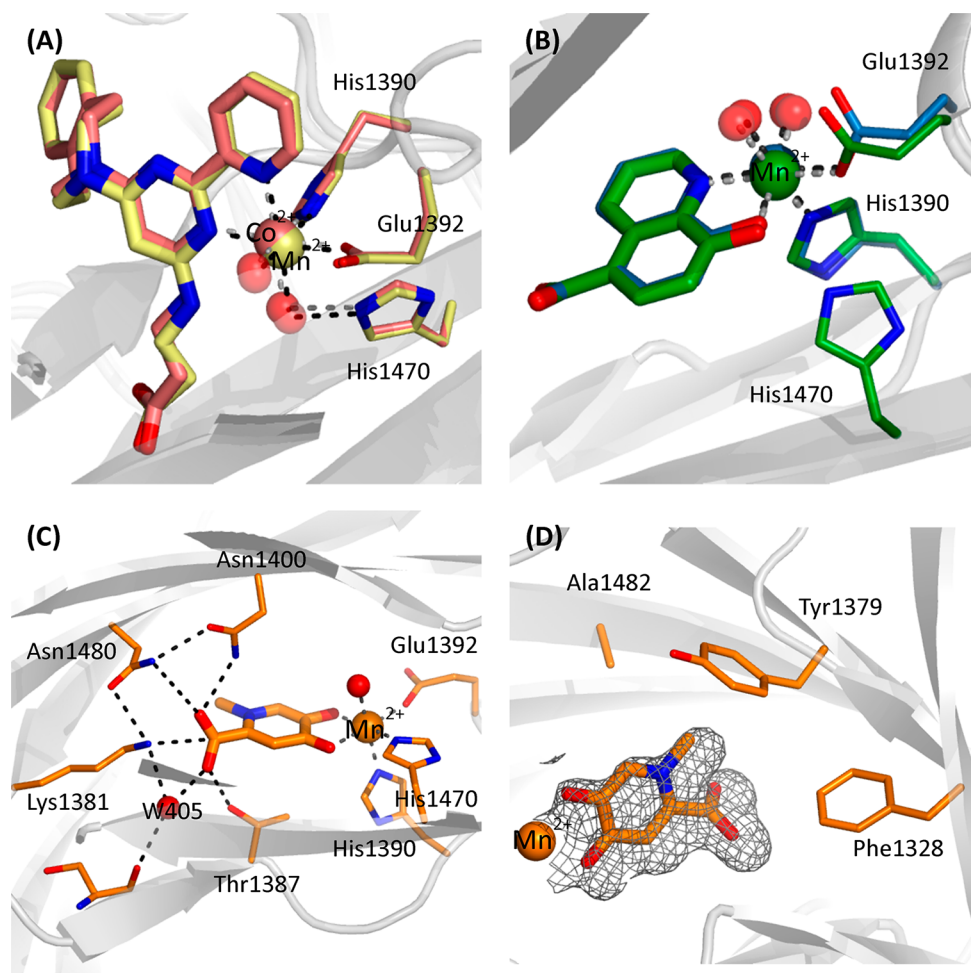


Figure 4. Protein X-ray crystallography analysis. (A, B) Comparison of holo crystal structures of UTX and JMJD3, and (C, D) binding mode of compound **8** in UTX. The structural overlap of (A) UTX (PDB code: 6G8F) and JMJD3 (PDB code: 4ASK) in complex with GSK-J1 and (B) the overlap of the complexes with 5C8HQ (6FUK and 2XXZ) show that the binding mode is essentially identical in the two cognate enzymes, and thus, UTX can be used as surrogate in crystallography analysis of JMJD3 inhibitors. (C, D) Compound **8** forms with UTX both polar and nonpolar interactions through its carboxyl group and *N*-methyl substituent, respectively (PDB code: 6FUL). The 2Fo-Fc electron density map is shown by a mesh contoured at 1σ . Only the scaffold that chelates the catalytic metal had well-defined electron density. Thus, the methoxyphenyl moiety of **8** is not shown. Residue numbering corresponds to the sequence in JMJD3 to be consistent with the main text. The corresponding residues in UTX are Phe1084 (instead of Phe1328), Tyr1135 (Tyr1379), Lys1137 (Lys1381), Thr1143 (Thr1387), His1146 (His1390), Glu1148 (Glu1392), Asn1156 (Asn1400), His1226 (His1470), Asn1236 (Asn1480), and Ala1238 (Ala1482).

servers, respectively. All inhibitors passed the PAINS filters, while compounds **10–13** exhibited similarity to two known aggregators (Table S4). Nevertheless, the Tanimoto similarity between compounds **10–13** and the known aggregators, calculated using the Similarity Workbench of ChemMine tools,⁷⁷ does not exceed 0.50 (Table S4).

X-ray Crystallography. We carried out initial unsuccessful crystallization attempts on the JmjC domain of JMJD3, which prompted us to perform crystallization studies on the UTX construct, containing also the GATA-like zinc finger domain. Since the catalytic domain is highly conserved among KDM6 proteins, we assumed that JMJD3 inhibitors have a similar binding mode in UTX. As a proof of concept, the crystal structures of the UTX/GSK-J1 and UTX/5C8HQ complexes were solved by molecular replacement and refined to a resolution of 2.05 and 2.00 Å, respectively (PDB codes: 6G8F and 6FUK, Figure S12). Superimpositions of the JMJD3 and UTX complex structures based on the $C\alpha$ atoms showed that GSK-J1 heavy atoms overlap with a RMSD of 0.3 Å (Figure 4A), and 5C8HQ heavy atoms overlap with a RMSD of 0.06 Å (Figure 4B). As observed

in the case of JMJD3, the binding of GSK-J1 and 5C8HQ induces a metal movement of about 2 Å, relative to the *N*-oxalylglycine (NOG) bound structure (PDB code: 3AVS, Figure S13).⁹ This movement is accompanied by the displacement of His1470 away from the coordination shell, which is completed by either a water molecule in the case of GSK-J1 or the phenolic oxygen of the ligand in the case of 5C8HQ.

The structure of compound **8** in complex with UTX was obtained by soaking experiments (1.65 Å resolution, PDB code 6FUL). Statistics on X-ray diffraction data and the final model are reported in Table S3. Although the electron density map revealed unambiguous positions for the metal-chelating substructure, the 2-methoxyphenyl group lacked defined density and could not be modeled (Figure 4D). In order to verify that compound **8** was free of impurities, NMR and HPLC experiments were carried out. Both experiments did not show any impurity peak (Figure S14). In addition, the chemical stability of compound **8** in the crystallization conditions, i.e., in the presence of UTX and manganese (Mn^{2+}), was investigated by LC-UV/MS. As shown in Figure S16, the main peak in the mass

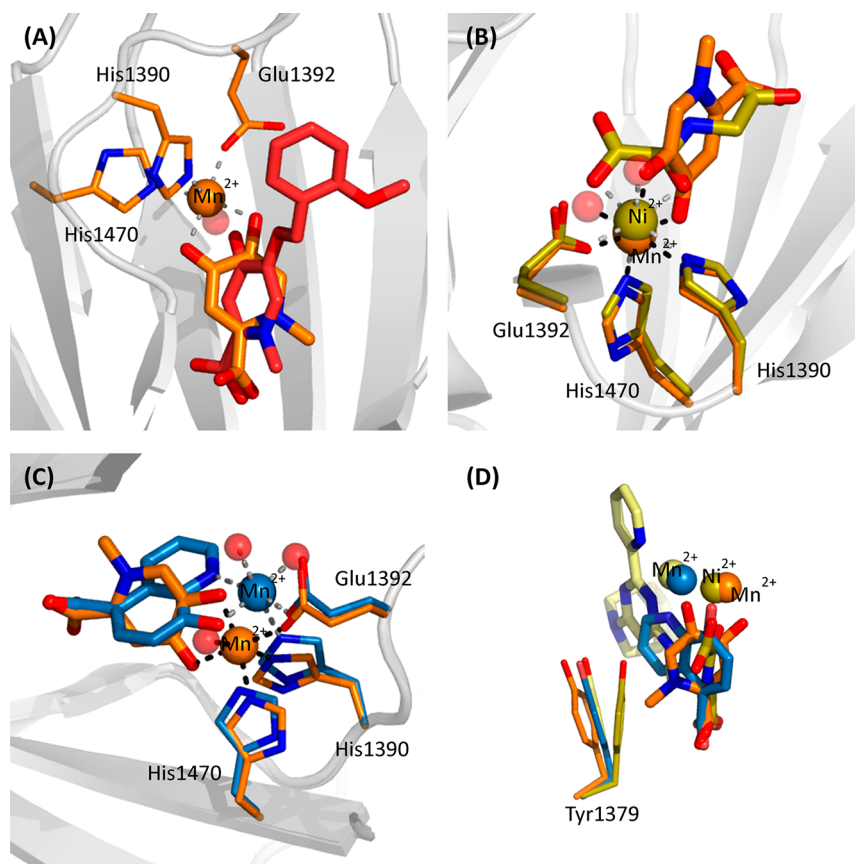


Figure 5. Comparison of binding mode of compound **8** with previously reported JMJD3 inhibitors. (A) Overlap of the crystallographic structure obtained by soaking experiments in UTX (carbon atoms in orange) and the predicted pose in JMJD3 (carbon atoms in red). Metal-coordination rearrangement upon binding of compound **8** to UTX (PDB code: 6FUL) compared to the binding of (B) NOG to UTX (PDB code: 3AVS) and (C) 5C8HQ to UTX (PDB code: 6FUK). (D) Comparison of the binding mode of compound **8** to UTX (orange) with previously reported inhibitors NOG (olive green), 5C8HQ (blue), and GSK-J1 (yellow, PDB code: 6G8F). The phenyl ring of Tyr1379 shows different orientations for different ligands, while the position of the carboxyl group of the inhibitors is conserved.

spectra corresponds to compound **8**, while no peak relative to the metal-chelating fragment (3-hydroxy-*L*-methyl-4-oxopyridine-6-carboxylic acid) was detected. These results support the hypothesis that the lack of electron density in the crystal structure is due to disordered binding of the 2-methoxyphenyl group.

As predicted by the pharmacophore-based pose, compound **8** makes a bidentate interaction with the metal ion Mn^{2+} through the carbonyl and ether oxygen atoms O2 and O4 (Figure 4C). Metal-binding through phenolic ether oxygen atoms is not common. For example, among the 96 chelating fragments reported by Jacobsen et al.,⁶⁰ only two of them present an ether group.

The carboxyl group of compound **8** is involved in electrostatic interactions with Lys1381, direct hydrogen bonds with Thr1387, Asn1400, and Asn1480, and a water-mediated hydrogen bond with the backbone carboxyl oxygen of Ser1385. Superposition of the crystal structure with the predicted pose shows that although the pyridine ring is tilted by about 40 degrees the described key features of the binding are conserved (Figure 5A). Consistently, the same tilting is observed while superposing the crystal structures of compound **8** and 5C8HQ, which was used for the pharmacophore-based pose generation (Figure 5C).

The structural overlap of the UTX structures in complex with compound **8** and NOG (PDB code: 3AVS) revealed that the bidentate chelation of compound **8** occurs in a plane orthogonal

to the one occupied by NOG (Figure 5B). This swapping between axial and equatorial positions is accompanied by a rearrangement of water molecules in the metal coordination. Interestingly, analysis of superposed UTX structures in complex with compound **8**, NOG, GSK-J1, and 5C8HQ, shows that the position of the shared carboxyl group is highly conserved (Figure 5D). Conversely, the flexibility of Tyr1379 and the variability of the metal coordination allow for the accommodation of different ligands (Figure 5D).

DISCUSSION

We have introduced a multistep protocol for *in silico* screening of compounds that bind to the catalytic metal of demethylases. In the first campaign, we docked into the JMJD3 demethylase a library of derivatives of known iron-chelating scaffolds. This led to the identification of compound **1** (Table 1). Subsequent SAR studies supported the predicted binding mode of hit **1** and resulted in four additional inhibitors (compounds **2–4** and **7**). These inhibitors to two different chemical classes and have IC_{50} values in the range from 10 to 100 μM . The successful results of the first campaign prompted us to apply the developed strategy for the identification of novel inhibitors. The second *in silico* screening resulted in the six inhibitors **8–12** and **14** (all with $IC_{50} < 100 \mu M$) containing three novel metal-chelating substructures. The hit rate is 30% (six actives of 20 compounds tested *in vitro*). A variety of high-throughput techniques have

been applied to lysine demethylases over the years^{78,79} such as RapidFire mass spectrometry,³⁰ Alphascreen,⁸⁰ and enzymatic formaldehyde dehydrogenase coupled assay.³² However, these techniques could hardly attain hit rates higher than 2%. Thus, the *in silico* screening compares favorably with experimental high-throughput campaigns.

Prior structural knowledge was used for the first screening campaign. For the second screening campaign, libraries of novel potential bidentate metal–ligands were first assembled by either substructure or pharmacophore search using information on known metal binders. Structural information was then retrieved from crystal structures and was used for pose generation to ensure proper geometry of the metal–ligand binding in the active site. In practice, this was achieved by aligning molecular conformers to the crystallographic known inhibitor scaffold pose by either tethered or pharmacophore docking (see *Methods*). Importantly, pharmacophore modeling was used for both library and pose generation during the second campaign (Figure 1, steps 1 and 2). This approach brings several advantages to the virtual screening workflow. As previously mentioned, the use of pharmacophores allows for the identification of novel inhibitors. Most importantly, the ability of pharmacophore-based docking to preserve interactions which are essential for the binding to the catalytic metal makes the developed strategy applicable to other metallo-proteins. However, to assess the transferability of the protocol, future work should involve benchmark studies on different classes of metallo-proteins which goes beyond the main purpose of the present work. Conformers which cannot fit the pharmacophore map are filtered out during pose generation (step 2) and do not undergo further screening, reducing significantly the computational cost. This step offers a significant improvement compared to previously reported virtual screening campaigns against KDM,^{81,82} in which proper metal–ligand binding was ensured by visual inspection only at the step of compounds selection.

It is important to note that the virtual screening protocols employed in this work suffer from three major drawbacks, which are inherent to the use of prior knowledge for pose generation. Both tethered docking and pharmacophore-based docking require the availability of an accurate protein structure, usually crystallographic or NMR. Second, the poses generated by substructure or feature alignment are biased by the input reference structure. Third, an exhaustive ensemble of conformations is needed for each of the ligands prior to pose generation. To serve this purpose, ChemAxon and RDKit conformer generators were used for the first and second campaign, respectively (see *Methods*). The choice of RDKit for the second campaign was based on a recent study from Friedrich et al.,⁶³ where the RDKit ensemble generator is shown to reproduce more than 80% of all protein-bound ligand conformations with an RMSD of less than 1 Å.

The protocol used in this work consisted of three steps for generating poses (steps 1–3 in Figure 1) and two successive steps for filtering and accurate scoring, respectively. The binding energy used for the final ranking is based on a transferable force field consisting of van der Waals energy and electrostatics with solvation evaluated by finite-difference Poisson calculation. The numerical solution of the Poisson equation discretized on a grid is computationally demanding for a protein like JMJD3 even if only the catalytic domain (292 residues) was considered for the calculation. Using focusing with initial and final grid spacing of 1.0 and 0.3 Å, respectively, the finite-difference Poisson calculation required an average of 6 min on a single core of a Xeon E5-2695 v4 CPU. To reduce the computational cost of the

finite-difference Poisson calculation, the number of poses was reduced (by factors of about 12 and 6 in the first and second campaigns, respectively) by the application of filters on the interaction energy between molecular conformers and QM probes. The use of semiempirical interaction energy as filters allowed for retaining only conformers involved in favorable interactions with polar groups of the binding site and was essential for speeding up the virtual screening protocol. It is important to note that while *ab initio* QM methods are computationally expensive and inapplicable to high-throughput screenings semiempirical methods are able to capture charge transfer and polarization effects at a low computational cost. In detail, the calculation of a single IE_{probe} took, on a commodity computer running Linux (Core i7 CPU with 3.07 GHz x8 and 24 GB RAM), an average of 0.2 s for rigid probes and of 0.65 s for flexible probes.

The X-ray crystal structure of compound 8 in complex with the UTX demethylase provided the validation for the binding to the catalytic metal. While the metal-binding fragment was well-defined in the electron density map (Figure 4D), we did not observe excess electron density that could be attributed to the 2-methoxyphenyl group. Metal-binding through an ether oxygen is unexpected. For this reason, we carried out a series of experiments to investigate the purity and stability of compound 8. The NMR spectra and HPLC-UV chromatogram (Figure S14) show that compound 8 is pure, while the LC-UV/MS data provide evidence that it does not undergo cleavage in the conditions used for the crystallography experiments (Figure S16). Three interesting observations emerge from the crystal structures with UTX which belongs to the same KDM6 subfamily as JMJD3. First, UTX can be used as a surrogate system for the crystallographic validation of the binding mode of compound 8 in JMJD3. Indeed, the superposition of the X-ray structures of UTX and JMJD3 provided evidence for the conserved binding modes of the two known inhibitors GSK-J1 and 5C8HQ (Figure 4A,B). Second, the position of the carboxyl group of different ligands is highly conserved in all crystal structures irrespective of the scaffold type (Figure 5D). On the contrary, the metal coordination is not rigid. The ligand can occupy both axial and equatorial positions, and the bond between the imidazole of His1470 and the catalytic iron can be either direct as for compound 8 and NOG or water mediated as for 5C8HQ and GSK-J1 (Figure 5B,C). Third, the phenyl ring of Tyr1379 shows different orientations, which allow for the accommodation of different ligands (Figure 5D).

CONCLUSIONS

To identify new JMJD3 demethylase inhibitors, we have carried out two *in silico* screening campaigns based on tethered docking and a 3D-pharmacophore search, respectively. The predicted poses were filtered by semiempirical QM evaluation of binding energy and ranked by a force field-based energy with an implicit solvent using the continuum dielectric approximation (finite-difference Poisson equation). A total of 11 inhibitors of JMJD3 ($IC_{50} < 100 \mu M$) belonging to five different chemical classes have been identified. The crystal structure in the complex with the UTX demethylase and favorable ligand efficiency of 0.32 kcal/mol per nonhydrogen atom make compound 8 a promising candidate for future optimization.

ASSOCIATED CONTENT

Supporting Information

The Supporting Information is available free of charge on the ACS Publications website at DOI: 10.1021/acs.jcim.8b00539.

Interaction energy values between known inhibitors and selected QM probes (Table S1), interaction energy values distributions (Figures S3 and S4), single-dose measurements (Table S2), and dose–response curves (Figures S9 and S11) by AlphaScreen assay, chemical structures of compounds inactive by AlphaScreen assay (Figures S6 and S8), X-ray crystallization data (Table S3), electron density maps of GSK-J1 and 5C8HQ (Figure S12), overlaps between JMJD3 and UTX crystal structures (Figure S13), tautomeric and protonation equilibria of compounds 8 and 9 (Figure S15), NMR spectra HPLC-UV chromatogram, and LC-UV/MS spectra of compound 8 (Figures S14 and S16). (PDF)

AUTHOR INFORMATION

Corresponding Author

*E-mail: caflisch@bioc.uzh.ch.

ORCID

C. Esposito: 0000-0003-3232-271X

A. Caflisch: 0000-0002-2317-6792

Notes

The authors declare no competing financial interest.

ACKNOWLEDGMENTS

We thank Aymeric Dolbois for carrying out NMR and HPLC experiments and Andrea Meier for LC-UV/MS. We thank Pawel Sledz and Dimitrios Spiliotopoulos for technical support and interesting discussions. We thank an anonymous reviewer for useful and interesting suggestions. We are grateful to the RIKEN Systems and Structural Biology Center and to Prof. Michael Gajhede and Sarah Elizabeth Jones of the University of Copenhagen for providing us two different plasmids of UTX (880-1401). We thank the Kazusa DNA Research Institute for the clone of the plasmid received from the RIKEN institute. Diffraction data were acquired on the PXI and PXIII beamlines, Swiss Light Source, Paul Scherrer Institute (Villigen, Switzerland). The finite-difference Poisson calculations were carried out on the Piz Daint supercomputer at the Swiss Center of Scientific Computing in Lugano. This work was supported financially by the Swiss National Science Foundation (Grant 31003A_169007 to A.C.).

REFERENCES

- (1) Klose, R. J.; Kallin, E. M.; Zhang, Y. Jmjc-Domain-Containing Proteins and Histone Demethylation. *Nat. Rev. Genet.* **2006**, *7*, 715.
- (2) D'Oto, A.; Tian, Q.-w.; Davidoff, A. M.; Yang, J. Histone Demethylases and Their Roles in Cancer Epigenetics. *J. Med. Oncol. Ther.* **2016**, *1*, 34.
- (3) Kooistra, S. M.; Helin, K. Molecular Mechanisms and Potential Functions of Histone Demethylases. *Nat. Rev. Mol. Cell Biol.* **2012**, *13*, 297.
- (4) Mosammamaparast, N.; Shi, Y. Reversal of Histone Methylation: Biochemical and Molecular Mechanisms of Histone Demethylases. *Annu. Rev. Biochem.* **2010**, *79*, 155–179.
- (5) Agger, K.; Cloos, P. A.; Christensen, J.; Pasini, D.; Rose, S.; Rappasilber, J.; Issaeva, I.; Canaani, E.; Salcini, A. E.; Helin, K. Utx and Jmjd3 Are Histone H3k27 Demethylases Involved in Hox Gene Regulation and Development. *Nature* **2007**, *449*, 731.
- (6) Greer, E. L.; Shi, Y. Histone Methylation: A Dynamic Mark in Health, Disease and Inheritance. *Nat. Rev. Genet.* **2012**, *13*, 343–357.
- (7) Burchfield, J. S.; Li, Q.; Wang, H. Y.; Wang, R.-F. Jmjd3 as an Epigenetic Regulator in Development and Disease. *Int. J. Biochem. Cell Biol.* **2015**, *67*, 148–157.
- (8) De Santa, F.; Totaro, M. G.; Prosperini, E.; Notarbartolo, S.; Testa, G.; Natoli, G. The Histone H3 Lysine-27 Demethylase Jmjd3

Links Inflammation to Inhibition of Polycomb-Mediated Gene Silencing. *Cell* **2007**, *130*, 1083–1094.

(9) Kruidenier, L.; Chung, C.-w.; Cheng, Z.; Liddle, J.; Che, K.; Joberty, G.; Bantscheff, M.; Bountra, C.; Bridges, A.; Diallo, H.; et al. A Selective Jumoni H3k27 Demethylase Inhibitor Modulates the Proinflammatory Macrophage Response. *Nature* **2012**, *488*, 404.

(10) Tang, Y.; Li, T.; Li, J.; Yang, J.; Liu, H.; Zhang, X.; Le, W. Jmjd3 Is Essential for the Epigenetic Modulation of Microglia Phenotypes in the Immune Pathogenesis of Parkinson's Disease. *Cell Death Differ.* **2014**, *21*, 369.

(11) Arcipowski, K. M.; Martinez, C. A.; Ntziachristos, P. Histone Demethylases in Physiology and Cancer: A Tale of Two Enzymes, Jmjd3 and Utx. *Curr. Opin. Genet. Dev.* **2016**, *36*, 59–67.

(12) Ntziachristos, P.; Tsirigou, A.; Welstead, G.; Trimarchi, T.; Bakogianni, S.; Xu, L.; Loizou, E.; Holmfeldt, L.; Strikoudis, A.; King, B.; et al. Contrasting Roles for Histone 3 Lysine 27 Demethylases in Acute Lymphoblastic Leukemia. *Nature* **2014**, *514*, 513.

(13) Heinemann, B.; Nielsen, J. M.; Hudlebusch, H. R.; Lees, M. J.; Larsen, D. V.; Boesen, T.; Labelle, M.; Gerlach, L.-O.; Birk, P.; Helin, K. Inhibition of Demethylases by Gsk-J1/J4/Kruidenier Et Al. Reply. *Nature* **2014**, *514*, E1.

(14) Hu, J.; Wang, X.; Chen, L.; Huang, M.; Tang, W.; Zuo, J.; Liu, Y.-C.; Shi, Z.; Liu, R.; Shen, J.; Xiong, B. Design and Discovery of New Pyrimidine Coupled Nitrogen Aromatic Rings as Chelating Groups of Jmjd3 Inhibitors. *Bioorg. Med. Chem. Lett.* **2016**, *26*, 721–725.

(15) Nowak, R. P.; Tumber, A.; Johansson, C.; Che, K. H.; Brennan, P.; Owen, D.; Oppermann, U. Advances and Challenges in Understanding Histone Demethylase Biology. *Curr. Opin. Chem. Biol.* **2016**, *33*, 151–159.

(16) McAllister, T. E.; England, K. S.; Hopkinson, R. J.; Brennan, P. E.; Kawamura, A.; Schofield, C. J. Recent Progress in Histone Demethylase Inhibitors. *J. Med. Chem.* **2016**, *59*, 1308–1329.

(17) Sliwoski, G.; Kothiwale, S.; Meiler, J.; Lowe, E. W. Computational Methods in Drug Discovery. *Pharmacol. Rev.* **2014**, *66*, 334–395.

(18) Śledź, P.; Caflisch, A. Protein Structure-Based Drug Design: From Docking to Molecular Dynamics. *Curr. Opin. Struct. Biol.* **2018**, *48*, 93–102.

(19) Seebeck, B.; Reulecke, I.; Kämper, A.; Rarey, M. Modeling of Metal Interaction Geometries for Protein–Ligand Docking. *Proteins: Struct., Funct., Genet.* **2008**, *71*, 1237–1254.

(20) Englebienne, P.; Fiaux, H.; Kuntz, D. A.; Corbeil, C. R.; Gerber-Lemaire, S.; Rose, D. R.; Moitessier, N. Evaluation of Docking Programs for Predicting Binding of Golgi A-Mannosidase Ii Inhibitors: A Comparison with Crystallography. *Proteins: Struct., Funct., Genet.* **2007**, *69*, 160–176.

(21) Santos-Martins, D.; Forli, S.; Ramos, M. J. o.; Olson, A. J. Autodock4zn: An Improved Autodock Force Field for Small-Molecule Docking to Zinc Metalloproteins. *J. Chem. Inf. Model.* **2014**, *54*, 2371–2379.

(22) Ballante, F.; Marshall, G. R. An Automated Strategy for Binding-Pose Selection and Docking Assessment in Structure-Based Drug Design. *J. Chem. Inf. Model.* **2016**, *56*, 54–72.

(23) Böhm, H.-J. The Development of a Simple Empirical Scoring Function to Estimate the Binding Constant for a Protein-Ligand Complex of Known Three-Dimensional Structure. *J. Comput.-Aided Mol. Des.* **1994**, *8*, 243–256.

(24) Gohlke, H.; Hendlich, M.; Klebe, G. Knowledge-Based Scoring Function to Predict Protein-Ligand Interactions. *J. Mol. Biol.* **2000**, *295*, 337–356.

(25) Moitessier, N.; Englebienne, P.; Lee, D.; Lawandi, J.; Corbeil, C. R. Towards the Development of Universal, Fast and Highly Accurate Docking/Scoring Methods: A Long Way to Go. *British journal of pharmacology* **2008**, *153* (153), S7–S26.

(26) Jain, T.; Jayaram, B. Computational Protocol for Predicting the Binding Affinities of Zinc Containing Metalloprotein–Ligand Complexes. *Proteins: Struct., Funct., Genet.* **2007**, *67*, 1167–1178.

(27) Kumari, T.; Issar, U.; Kakkar, R. Docking Modes of Bb-3497 into the Pdf Active Site—a Comparison of the Pure Mm and Qm/Mm Based Docking Strategies. *Curr. Comput.-Aided Drug Des.* **2015**, *10*, 315–326.

- (28) Bobovská, A.; Tvaroška, I.; Kóna, J. Using Dft Methodology for More Reliable Predictive Models: Design of Inhibitors of Golgi A-Mannosidase II. *J. Mol. Graphics Modell.* **2016**, *66*, 47–57.
- (29) Raha, K.; Merz, K. M. A Quantum Mechanics-Based Scoring Function: Study of Zinc Ion-Mediated Ligand Binding. *J. Am. Chem. Soc.* **2004**, *126*, 1020–1021.
- (30) Hutchinson, S. E.; Leveridge, M. V.; Heathcote, M. L.; Francis, P.; Williams, L.; Gee, M.; Munoz-Muriedas, J.; Leavens, B.; Shillings, A.; Jones, E.; et al. Enabling Lead Discovery for Histone Lysine Demethylases by High-Throughput Rapidfire Mass Spectrometry. *J. Biomol. Screening* **2012**, *17*, 39–48.
- (31) Yu, V.; Fisch, T.; Long, A. M.; Tang, J.; Lee, J. H.; Hierl, M.; Chen, H.; Yakowec, P.; Schwandner, R.; Emkey, R. High-Throughput Tr-FRET Assays for Identifying Inhibitors of Lsd1 and Jmjd2c Histone Lysine Demethylases. *J. Biomol. Screening* **2012**, *17*, 27–38.
- (32) King, O. N.; Li, X. S.; Sakurai, M.; Kawamura, A.; Rose, N. R.; Ng, S. S.; Quinn, A. M.; Rai, G.; Mott, B. T.; Beswick, P.; et al. Quantitative High-Throughput Screening Identifies 8-Hydroxyquinolines as Cell-Active Histone Demethylase Inhibitors. *PLoS One* **2010**, *5*, e15535.
- (33) Hopkinson, R. J.; Tumber, A.; Yapp, C.; Chowdhury, R.; Aik, W.; Che, K. H.; Li, X. S.; Kristensen, J. B.; King, O. N.; Chan, M. C.; et al. 5-Carboxy-8-Hydroxyquinoline Is a Broad Spectrum 2-Oxoglutarate Oxygenase Inhibitor Which Causes Iron Translocation. *Chem. Sci.* **2013**, *4*, 3110–3117.
- (34) Horvath, D. Pharmacophore-Based Virtual Screening. *Methods Mol. Biol.* **2010**, *672*, 261–298.
- (35) Sun, H. Pharmacophore-Based Virtual Screening. *Curr. Med. Chem.* **2008**, *15*, 1018–1024.
- (36) Sunseri, J.; Koes, D. R. Pharmit: Interactive Exploration of Chemical Space. *Nucleic Acids Res.* **2016**, *44*, W442–W448.
- (37) Brooks, B. R.; Brooks, C. L.; MacKerell, A. D.; Nilsson, L.; Petrella, R. J.; Roux, B.; Won, Y.; Archontis, G.; Bartels, C.; Boresch, S.; et al. Charmm: The Biomolecular Simulation Program. *J. Comput. Chem.* **2009**, *30*, 1545–1614.
- (38) Huang, J.; MacKerell, A. D. CHARMM36 All-Atom Additive Protein Force Field: Validation Based on Comparison to NMR Data. *J. Comput. Chem.* **2013**, *34*, 2135–2145.
- (39) Vanommeslaeghe, K.; Raman, E. P.; MacKerell, A. D. Automation of the CHARMM General Force Field (CGenFF) II: Assignment of Bonded Parameters and Partial Atomic Charges. *J. Chem. Inf. Model.* **2012**, *52*, 3155–3168.
- (40) Marchand, J.-R.; Dalle Vedove, A.; Lolli, G.; Caflich, A. Discovery of Inhibitors of Four Bromodomains by Fragment-Anchored Ligand Docking. *J. Chem. Inf. Model.* **2017**, *57*, 2584–2597.
- (41) Zhou, T.; Caflich, A. High-Throughput Virtual Screening Using Quantum Mechanical Probes: Discovery of Selective Kinase Inhibitors. *ChemMedChem* **2010**, *5*, 1007–1014.
- (42) Stewart, J. J. Mopac: A Semiempirical Molecular Orbital Program. *J. Comput.-Aided Mol. Des.* **1990**, *4*, 1–103.
- (43) Stewart, J. J. Optimization of Parameters for Semiempirical Methods VI: More Modifications to the Nddo Approximations and Re-Optimization of Parameters. *J. Mol. Model.* **2013**, *19*, 1–32.
- (44) Huang, D.; Caflich, A. Efficient Evaluation of Binding Free Energy Using Continuum Electrostatics Solvation. *J. Med. Chem.* **2004**, *47*, 5791–5797.
- (45) Im, W.; Beglov, D.; Roux, B. Continuum Solvation Model: Computation of Electrostatic Forces from Numerical Solutions to the Poisson-Boltzmann Equation. *Comput. Phys. Commun.* **1998**, *111*, 59–75.
- (46) Lin, F.; Wang, R. Systematic Derivation of Amber Force Field Parameters Applicable to Zinc-Containing Systems. *J. Chem. Theory Comput.* **2010**, *6*, 1852–1870.
- (47) Vedani, A.; Huhta, D. W. A New Force Field for Modeling Metalloproteins. *J. Am. Chem. Soc.* **1990**, *112*, 4759–4767.
- (48) Stote, R. H.; Karplus, M. Zinc Binding in Proteins and Solution: A Simple but Accurate Nonbonded Representation. *Proteins: Struct., Funct., Genet.* **1995**, *23*, 12–31.
- (49) Åqvist, J. Modelling of Ion-Ligand Interactions in Solutions and Biomolecules. *J. Mol. Struct.: THEOCHEM* **1992**, *256*, 135–152.
- (50) Aqvist, J.; Warshel, A. Free Energy Relationships in Metalloenzyme-Catalyzed Reactions. Calculations of the Effects of Metal Ion Substitutions in Staphylococcal Nuclease. *J. Am. Chem. Soc.* **1990**, *112*, 2860–2868.
- (51) Oelschlaeger, P.; Klahn, M.; Beard, W. A.; Wilson, S. H.; Warshel, A. Magnesium-Cationic Dummy Atom Molecules Enhance Representation of DNA Polymerase B in Molecular Dynamics Simulations: Improved Accuracy in Studies of Structural Features and Mutational Effects. *J. Mol. Biol.* **2007**, *366*, 687–701.
- (52) Pang, Y.-P. Novel Zinc Protein Molecular Dynamics Simulations: Steps toward Antiangiogenesis for Cancer Treatment. *J. Mol. Model.* **1999**, *5*, 196–202.
- (53) Calculator Plugins Were Used for Structure Property Prediction and Calculation, 2015. Marvin 15.1.5.0, Chemaxon. www.chemaxon.com (accessed 2018).
- (54) Allscher, T.; Klüfers, P.; Mayer, P. Carbohydrate-Metal Complexes Carbohydrate–Metal Complexes: Structural Chemistry of Stable Solution Species. In *Glycoscience*; Springer: 2008; pp 1077–1139.
- (55) Chandra, I. K.; Angkawijaya, A. E.; Santoso, S. P.; Ismadji, S.; Soetaredjo, F. E.; Ju, Y.-H. Solution Equilibria Studies of Complexes of Divalent Metal Ions with 2-Aminophenol and 3, 4-Dihydroxybenzoic Acid. *Polyhedron* **2015**, *88*, 29–39.
- (56) O’Boyle, N. M.; Banck, M.; James, C. A.; Morley, C.; Vandermeersch, T.; Hutchison, G. R. Open Babel: An Open Chemical Toolbox. *J. Cheminf.* **2011**, *3*, 33.
- (57) Ruiz-Carmona, S.; Alvarez-Garcia, D.; Foppe, N.; Garmendia-Doval, A. B.; Juhos, S.; Schmidtke, P.; Barril, X.; Hubbard, R. E.; Morley, S. D. Rdock: A Fast, Versatile and Open Source Program for Docking Ligands to Proteins and Nucleic Acids. *PLoS Comput. Biol.* **2014**, *10*, e1003571.
- (58) Yesselman, J. D.; Price, D. J.; Knight, J. L.; Brooks, C. L. Match: An Atom-Typing Toolset for Molecular Mechanics Force Fields. *J. Comput. Chem.* **2012**, *33*, 189–202.
- (59) Vitalis, A.; Caflich, A. Efficient Construction of Mesostate Networks from Molecular Dynamics Trajectories. *J. Chem. Theory Comput.* **2012**, *8*, 1108–1120.
- (60) Jacobsen, J. A.; Fullagar, J. L.; Miller, M. T.; Cohen, S. M. Identifying Chelators for Metalloprotein Inhibitors Using a Fragment-Based Approach. *J. Med. Chem.* **2011**, *54*, 591–602.
- (61) Papadopoulos, A. G.; Charistos, N. D.; Muñoz-Castro, A. On the Role of Heteroatoms in Aromatic Rings. Insights from 10 π Main Group Elements Heterorings [(Eh) 2 S 2 N 4] Q (E= C, P, B, Si, Al and Q= 0, –2). *New J. Chem.* **2016**, *40*, 5090–5098.
- (62) Le, G.; Vandegraaff, N.; Rhodes, D. I.; Jones, E. D.; Coates, J. A.; Thienthong, N.; Winfield, L. J.; Lu, L.; Li, X.; Yu, C.; Feng, X.; Deadman, J. J. Design of a Series of Bicyclic Hiv-1 Integrase Inhibitors. Part 2: Azoles: Effective Metal Chelators. *Bioorg. Med. Chem. Lett.* **2010**, *20*, 5909–5912.
- (63) Friedrich, N.-O.; Meyder, A.; de Bruyn Kops, C.; Sommer, K.; Flachsenberg, F.; Rarey, M.; Kirchmair, J. High-Quality Dataset of Protein-Bound Ligand Conformations and Its Application to Benchmarking Conformer Ensemble Generators. *J. Chem. Inf. Model.* **2017**, *57*, 529–539.
- (64) Rappé, A. K.; Casewit, C. J.; Colwell, K.; Goddard, W., III; Skiff, W. Uff, a Full Periodic Table Force Field for Molecular Mechanics and Molecular Dynamics Simulations. *J. Am. Chem. Soc.* **1992**, *114*, 10024–10035.
- (65) Sengoku, T.; Yokoyama, S. Structural Basis for Histone H3 Lys 27 Demethylation by Utx/Kdm6a. *Genes Dev.* **2011**, *25*, 2266–2277.
- (66) Kristensen, J. B.; Nielsen, A. L.; Jørgensen, L.; Kristensen, L. H.; Helgstrand, C.; Juknaite, L.; Kristensen, J. L.; Kastrup, J. S.; Clausen, R. P.; Olsen, L.; Gajhede, M. Enzyme Kinetic Studies of Histone Demethylases Kdm4c and Kdm6a: Towards Understanding Selectivity of Inhibitors Targeting Oncogenic Histone Demethylases. *FEBS Lett.* **2011**, *585*, 1951–1956.
- (67) Kabsch, W. Integration, Scaling, Space-Group Assignment and Post Refinement. In *International Tables for Crystallography Vol. F:*

Crystallography of Biological Macromolecules; Springer: 2006; pp 218–225.

(68) McCoy, A. J.; Grosse-Kunstleve, R. W.; Adams, P. D.; Winn, M. D.; Storoni, L. C.; Read, R. J. Phaser Crystallographic Software. *J. Appl. Crystallogr.* **2007**, *40*, 658–674.

(69) Adams, P. D.; Afonine, P. V.; Bunkóczy, G.; Chen, V. B.; Davis, I. W.; Echols, N.; Headd, J. J.; Hung, L.-W.; Kapral, G. J.; Grosse-Kunstleve, R. W.; et al. Phenix: A Comprehensive Python-Based System for Macromolecular Structure Solution. *Acta Crystallogr., Sect. D: Biol. Crystallogr.* **2010**, *66*, 213–221.

(70) Emsley, P.; Lohkamp, B.; Scott, W. G.; Cowtan, K. Features and Development of Coot. *Acta Crystallogr., Sect. D: Biol. Crystallogr.* **2010**, *66*, 486–501.

(71) Ghosh, A. K.; Brindisi, M. Organic Carbamates in Drug Design and Medicinal Chemistry. *J. Med. Chem.* **2015**, *58*, 2895–2940.

(72) Baell, J. B.; Holloway, G. A. New Substructure Filters for Removal of Pan Assay Interference Compounds (PAINS) from Screening Libraries and for Their Exclusion in Bioassays. *J. Med. Chem.* **2010**, *53*, 2719–2740.

(73) McGovern, S. L.; Caselli, E.; Grigorieff, N.; Shoichet, B. K. A Common Mechanism Underlying Promiscuous Inhibitors from Virtual and High-Throughput Screening. *J. Med. Chem.* **2002**, *45*, 1712–1722.

(74) Lagorce, D.; Sperandio, O.; Baell, J. B.; Miteva, M. A.; Villoutreix, B. O. Faf-Drugs3: A Web Server for Compound Property Calculation and Chemical Library Design. *Nucleic Acids Res.* **2015**, *43*, W200–W207.

(75) Lagorce, D.; Bouzlama, L.; Becot, J.; Miteva, M. A.; Villoutreix, B. O. Faf-Drugs4: Free Adme-Tox Filtering Computations for Chemical Biology and Early Stages Drug Discovery. *Bioinformatics* **2017**, *33*, 3658–3660.

(76) Irwin, J. J.; Duan, D.; Torosyan, H.; Doak, A. K.; Ziebart, K. T.; Sterling, T.; Tumanian, G.; Shoichet, B. K. An Aggregation Advisor for Ligand Discovery. *J. Med. Chem.* **2015**, *58*, 7076–7087.

(77) Backman, T. W.; Cao, Y.; Girke, T. Chemmine Tools: An Online Service for Analyzing and Clustering Small Molecules. *Nucleic Acids Res.* **2011**, *39*, W486–W491.

(78) Gale, M.; Yan, Q. High-Throughput Screening to Identify Inhibitors of Lysine Demethylases. *Epigenomics* **2015**, *7*, 57–65.

(79) Ma, H.; Howitz, K. T.; Horiuchi, K. Y.; Wang, Y. Histone Methyltransferase Activity Assays. In *Epigenetics for Drug Discovery*; Royal Society of Chemistry: 2015; pp 267–287.

(80) Kawamura, A.; Tumber, A.; Rose, N. R.; King, O. N.; Daniel, M.; Oppermann, U.; Heightman, T. D.; Schofield, C. Development of Homogeneous Luminescence Assays for Histone Demethylase Catalysis and Binding. *Anal. Biochem.* **2010**, *404*, 86–93.

(81) Korczynska, M.; Le, D. D.; Younger, N.; Gregori-Puigjane, E.; Tumber, A.; Krojer, T.; Velupillai, S.; Gileadi, C.; Nowak, R. P.; Iwasa, E.; et al. Docking and Linking of Fragments to Discover Jumonji Histone Demethylase Inhibitors. *J. Med. Chem.* **2016**, *59*, 1580–1598.

(82) Chu, C.-H.; Wang, L.-Y.; Hsu, K.-C.; Chen, C.-C.; Cheng, H.-H.; Wang, S.-M.; Wu, C.-M.; Chen, T.-J.; Li, L.-T.; Liu, R.; et al. Kdm4b as a Target for Prostate Cancer: Structural Analysis and Selective Inhibition by a Novel Inhibitor. *J. Med. Chem.* **2014**, *57*, 5975–5985.